Ground Vehicle Navigation Integrity Monitoring for Multi-Constellation GNSS Fused with Cellular Signals of Opportunity

Mu Jia[1], Halim Lee[2], Joe Khalife[1], Zaher M. Kassas[1], and Jiwon Seo[2]

Abstract— **Integrity monitoring of a ground vehicle navigation system, utilizing multi-constellation global navigation satellite systems (GNSS) signals fused with ambient cellular signals of opportunity (SOPs) is considered. An advanced receiver autonomous integrity monitoring (ARAIM) framework is developed to detect and exclude multipath and non-line-of-sight errors. A method to conservatively predict the horizontal protection level (HPL) is proposed, utilizing ray-tracing and channel impulse response prediction in a three-dimensional (3D) building map of the environment. Simulation results are presented demonstrating the conservatively predicted HPL with different signals (GPS-only, GPS+GLONASS, GPS+SOP, and GPS+GLONASS+SOP). Experimental results are presented for a ground vehicle navigating a trajectory of 1380 m in an urban environment, showing the availability rates for GPS-only, GPS+GLONASS, GPS+SOP, and GPS+GLONASS+SOP being 52.53%, 75.66%, 76.87%, and 80.72%, respectively.**

I. Introduction

Passenger safety in ground vehicles depend on the accuracy and reliability of the vehicle's navigation system. This is particularly the case for semi- and fully-automated vehicles. Ground vehicle navigation systems utilize global navigation satellite systems (GNSS) receivers and a suite of onboard sensors, e.g., lidar, camera, radar, inertial navigation system (INS), etc. GNSS are relied upon to provide a navigation solution in a global frame and to correct for accumulating errors due to sensor dead reckoning.

While achieving higher levels of navigation accuracy has been a classic requirement, the trustworthiness in the navigation solution, commonly assessed by integrity measures, is evermore vital in the safety critical application of automated driving. To ensure safe navigation, automated vehicles need to tightly bound the navigation errors and ensure that the probability of navigation errors being not properly bounded is below a certain limit. Current GNSS technologies are insufficient to support the transition of ground vehicles to full automation in terms of accuracy, integrity, and availability [1]. In terms of accuracy, sub-meter-level accuracy is achievable with certain augmentation systems and real-time kinematic (RTK) only under certain favorable conditions [2]; while single point positioning (SPP) can only achieve meter-level accuracy [3]. In terms of integrity and availability, recent work demonstrated that in a sample downtown environment (Chicago urban corridor), availability of GPS-only positioning was less than 10% at most locations. While using multi-constellation GNSS (GPS, GLONASS, Galileo, and Beidou) improved the availability significantly, it was still lower than 80% at certain points; concluding that multi-constellation GNSS cannot provide continuous vehicle positioning along the street [4].

Recently, signals of opportunity (SOPs), e.g., cellular signals [5] and digital television signals [6], have been been demonstrated as an attractive alternative or supplement to GNSS signals. SOPs could provide a navigation solution in a global frame in a standalone fashion [7], [8] or aid dead reckoning sensors (e.g., INS [9]). For vehicular navigation in urban environments, cellular SOPs are particularly attractive due to their inherent attributes: abundance, geometric and spectral diversity, high received power, and large bandwidth. When used alongside GNSS signals, SOPs could improve the accuracy, integrity, and availability of the navigation system.

GNSS-based integrity monitoring has been studied extensively [10]. Among the proposed frameworks, receiver autonomous integrity monitoring (RAIM) is exceptionally attractive, as it is cost-effective and does not require building additional infrastructure [11]. RAIM has been adapted to account for multi-constellation GNSS measurements [12] (e.g. Galileo [13], GLONASS [14], and Beidou [15]), aiding sensors (e.g., INS-GPS [16], lidar-GNSS [17], and vision-GPS [18]), and terrestrial SOPs [19], [20]. An initial study to characterize the integrity monitoring improvement for automated driving, upon fusing GPS signals with terrestrial SOPs, was conducted in [21]. However, this study assumed fault-free measurements, which is not realistic in urban environments, in which multipath effects and non-line-of-sight (NLOS) conditions are prevalent. In [22], the protection level reduction due to fusing GPS and terrestrial SOPs was studied; however, multipath and NLOS effects in GNSS and SOP measurements were not explicitly considered.

This paper makes three contributions. First, an advanced RAIM (ARAIM) framework is proposed to incorporate multi-constellation GNSS and cellular long-term evolution (LTE) SOPs. Second, a method to conservatively predict the horizontal protection level (HPL) is proposed, utilizing ray-tracing and channel impulse response prediction in a three-dimensional (3D) building map of the environment. Third, simulation and experimental results are presented demonstrating the efficacy of fusing multi-constellation GNSS with cellular terrestrial SOPs in terms of reducing the HPL.

The rest of this paper is organized as follows. Section II

This work was supported in part by the U.S. Department of Transportation (USDOT) under Grant 69A3552047138 for the CARMEN University Transportation Center (UTC) and in part by the National Science Foundation (NSF) under Grant 1929965.

[1]Department of Mechanical and Aerospace Engineering, University of California, Irvine, muj2@uci.edu, khalifej@uci.edu, zkassas@ieee.org

[2]School of Integrated Technology, Yonsei University, Korea, halim.lee@yonsei.ac.kr, jiwon.seo@yonsei.ac.kr

describes the GNSS and cellular SOP pseudorange measurement models and estimator used to fuse these measurements. Section III formulates the method to conservatively predict the HPL. Section IV presents simulation and experimental results. Section V gives concluding remarks.

II. Model Description

This section describes the GNSS and cellular pseudorange measurement models and the weighted nonlinear least square (WNLS) estimator used to estimate the vehicle's position. Furthermore, this section provides an overview of the ARAIM algorithm for integrity monitoring with multi-constellation GNSS and cellular SOPs.

A. GNSS Pseudorange Measurement Model

The ground vehicle-mounted receiver makes pseudorange measurements to M GNSS satellites from N_{const} GNSS constellations. Let $i \in \{1, \ldots, N_{\text{const}}\}$ denote the index of the constellation to which the m-th GNSS satellite belongs. The m-th GNSS pseudorange measurement at time-step k, after compensating for ionospheric delays, tropospheric delays, and the satellite's clock bias, is modeled as

$$\begin{aligned} z_{\text{GNSS}_m}(k) =& \|\boldsymbol{r}_r(k) - \boldsymbol{r}_{\text{GNSS}_m}(k)\|_2 + c \cdot \delta t_{r,i}(k) \\ &+ b_{\text{GNSS}_m}(k) + v_{\text{GNSS}_m}(k), \end{aligned} \tag{1}$$

where $z_{\text{GNSS}_m}(k) = z'_{\text{GNSS}_m}(k) + c\hat{\delta}t_{\text{GNSS}_m}(k) - c \cdot \hat{\delta}t_{\text{iono}}(k) - c \cdot \hat{\delta}t_{\text{tropo}}(k)$; $z'_{\text{GNSS}_m}(k)$ is the pseudorange from the m-th GNSS satellite before corrections; c is the speed of light; $\hat{\delta}t_{\text{GNSS}_m}(k)$ is the m-th GNSS satellite's clock bias estimate; $\hat{\delta}t_{\text{iono}}(k)$ and $\hat{\delta}t_{\text{tropo}}(k)$ are the estimated ionospheric and tropospheric delays, respectively; $\boldsymbol{r}_r(k)$ and $\boldsymbol{r}_{GNSS_m}(k)$ are the receiver and m-th satellite's 3D position vectors, respectively; $\delta t_{r,i}(k)$ is the receiver's clock bias with respect to the i-th GNSS constellation's reference time; $b_{\text{GNSS}_m}(k)$ is the bias caused by multipath interference and/or NLOS effects; and v_{GNSS_m} is the measurement noise, which is modeled as a zero-mean, white Gaussian sequence with variance $\sigma^2_{\text{GNSS}_m}$. The prediction of $b_{\text{GNSS}_m}(k)$ via ray-tracing simulations is addressed in Section III-A.

B. Cellular SOP Pseudorange Measurement Model

The ground vehicle-mounted receiver also makes pseudorange measurements from N cellular base stations, which are assumed to be stationary with known positions. The n-th SOP measurement at time-step k can be modeled as

$$\begin{aligned} \bar{z}_{\text{SOP}_n} =& \|\boldsymbol{r}_r(k) - \boldsymbol{r}_{\text{SOP}_n}\|_2 + c \cdot [\bar{\delta}t_{r,\text{SOP}}(k) \\ &- \delta t_{\text{SOP}_n}(k)] + b_{\text{SOP}_n}(k) + \bar{v}_{\text{SOP}_n}(k), \end{aligned} \tag{2}$$

where $\boldsymbol{r}_{\text{SOP}_n}$ and $\delta t_{\text{SOP}_n}(k)$ are the position and clock bias of the n-th SOP transmitter with respect to cellular system time, respectively; $\bar{\delta}t_{r,\text{SOP}}(k)$ is the the receiver's clock bias with respect to cellular system time; $b_{\text{SOP}_n}(k)$ is the bias caused by multipath interference and/or NLOS effects for the SOP; and $\bar{v}_{\text{SOP}_n}$ is the measurement noise, which is modeled as a zero-mean white Gaussian sequence with variance $\sigma^2_{\text{user,SOP}_n}$. Based on [23], the difference $c \cdot [\bar{\delta}t_{r,\text{SOP}}(k) - \delta t_{\text{SOP}_n}(k)]$ can be modeled as

$$\begin{aligned} c \cdot [\bar{\delta}t_{r,\text{SOP}}(k) - \delta t_{\text{SOP}_n}(k)] =& c\delta t_{r,\text{SOP}}(k) + c\delta t_{\text{SOP}_n,0} \\ &+ \epsilon_n(k), \end{aligned} \tag{3}$$

where $c\delta t_{r,\text{SOP}}(k)$ is a common term driving the difference between the receiver and SOP clock biases, $c\delta t_{\text{SOP}_n,0}$ is an initial bias, and $\epsilon_n(k)$ is an error term modeled as a zero-mean Gaussian random variable with variance $\sigma^2_{\epsilon_n}$. It is assumed that the initial biases $\left\{c\delta t_{\text{SOP}_n,0}\right\}_{n=1}^{N}$ were calibrated prior to integrity monitoring. Finally, after initial bias calibration, the n-th SOP pseudorange measurement z_{SOP_n} can be expressed as

$$\begin{aligned} z_{\text{SOP}_n} =& \|\boldsymbol{r}_r(k) - \boldsymbol{r}_{\text{SOP}_n}(k)\|_2 + c\delta t_{r,\text{SOP}}(k) \\ &+ b_{\text{SOP}_n}(k) + v_{\text{SOP}_n}(k), \end{aligned} \tag{4}$$

where $v_{\text{SOP}_n}(k) \triangleq \epsilon_n(k) + \bar{v}_{\text{SOP}_n}(k)$. The variances for the noise terms are characterized in [22]. The prediction of the bias term for SOPs is discussed in Section III-B.

C. Navigation Solution

The ground vehicle estimates its position vector using GNSS and SOP pseudorange measurements via a WNLS. The vector to be estimated is given by

$$\boldsymbol{x}(k) \triangleq \left[\boldsymbol{r}_r{}^{\mathsf{T}}(k), c\delta t_{r,1}(k), \ldots, c\delta t_{r,N_{\text{const}}}(k), c\delta t_{r,\text{SOP}}(k)\right]^{\mathsf{T}}.$$

The time argument is omitted in the following for compactness of notation. The all-in-view combined GNSS-SOP measurement vector can be formed according to

$$\boldsymbol{z} \triangleq \left[z_{\text{GNSS}_1}, \ldots, z_{\text{GNSS}_M}, z_{\text{SOP}_1}, \ldots, z_{\text{SOP}_N}\right]^{\mathsf{T}}.$$

A WNLS is then iterated to obtain an estimate of $\boldsymbol{x}$, denoted by $\hat{\boldsymbol{x}}$, using $\boldsymbol{z}$. Let h denote the iteration number, $\hat{\boldsymbol{x}}_h$ the estimate at iteration h, and $\hat{\boldsymbol{z}}_h$ the measurement prediction calculated using $\hat{\boldsymbol{x}}_h$. The all-in-view navigation solution update is obtained from the normal equations according to

$$\Delta\boldsymbol{x}_h = \left(\mathbf{H}_h{}^{\mathsf{T}}\mathbf{W}\mathbf{H}_h\right)^{-1}\mathbf{H}_h{}^{\mathsf{T}}\mathbf{W}\left(\boldsymbol{z} - \hat{\boldsymbol{z}}_h\right), \tag{5}$$

where $\mathbf{H}_h$ is the measurement Jacobian evaluated at $\hat{\boldsymbol{x}}_h$ and $\mathbf{W}$ is the weight matrix. The weight matrix is given by $\mathbf{W} = \mathbf{C}_{\text{int}}^{-1}$, where $\mathbf{C}_{\text{int}}$ is a diagonal matrix whose diagonal elements $\left\{\mathbf{C}_{\text{int}}(j,j)\right\}_{j=1}^{N+M}$ are the measurement noise variances used for integrity. The WNLS estimate at the $(h+1)$-th iteration is updated according to

$$\hat{\boldsymbol{x}}_{h+1} = \hat{\boldsymbol{x}}_h + \Delta\boldsymbol{x}_h,$$

and the iteration number is subsequently increased according to $h \leftarrow h+1$. After convergence, the all-in-view navigation solution is denoted $\hat{\boldsymbol{x}}^{(\infty)}$, the measurement prediction after convergence is denoted $\hat{\boldsymbol{z}}^{(\infty)}$, and the residual at convergence is denoted $\boldsymbol{y}$, which is given by

$$\boldsymbol{y} \triangleq \boldsymbol{z} - \hat{\boldsymbol{z}}^{(\infty)}.$$

Let $\mathbf{H}$ denote the measurement Jacobian after convergence. $\mathbf{H}$ is an $(N+M) \times (3 + N_{\text{const}} + 1)$ matrix, which can be

parameterized by the GNSS satellites and SOP transmitters' azimuth and elevation angles as $\mathbf{H} \triangleq [\mathbf{G}, \mathbf{B}]$, where $\mathbf{G}$ is the geometry matrix, and $\mathbf{B}$ is the time matrix. The j-th row of $\mathbf{G}$ matrix can be defined as

$$\mathbf{G}_j \triangleq \left[-c(El_j)s(Az_j) \ -c(El_j)c(Az_j) \ -s(El_j)\right],$$

where $c(\cdot)$ and $s(\cdot)$ denote the $\cos(\cdot)$ and $\sin(\cdot)$ functions, respectively, and El_j and Az_j are elevation angle and azimuth angle, respectively, of j-th GNSS satellite or cellular base station. The clock bias Jacobian $\mathbf{B}$ can be expressed as

$$\mathbf{B} \triangleq \begin{bmatrix} \mathbf{B}' & \mathbf{0}_{M\times 1} \\ \mathbf{0}_{N\times N_{\text{const}}} & \mathbf{1}_{N\times 1} \end{bmatrix}, \tag{6}$$

where $\mathbf{B}'$ is an $M \times N_{\text{const}}$ matrix denoting the GNSS clock bias Jacobian, whose m, i-th entry, denoted by B'_{mi}, is

$$B'_{mi} = \begin{cases} 1 & \text{if } m\text{-th satellite belongs to } i\text{-th constellation,} \\ 0 & \text{otherwise.} \end{cases}$$

D. ARAIM with SOP Framework

This article extends the ARAIM with SOP framework proposed in [22] to incorporate multi-constellation GNSS and pseudorange measurements. ARAIM performs fault detection and exclusion (FDE) and HPL calculation based on the multiple hypothesis solution separation (MHSS) algorithm. The reasons for choosing ARAIM are twofold: (i) flexibility of the multiple-source ARAIM framework allows it to incorporate pseudorange measurements from different GNSS constellations and SOPs and (ii) due to the high probability of large biases caused by NLOS and multipath interference in urban environments, multiple faults should be considered.

III. Conservative HPL Prediction

This section describes the proposed method to analyze the performance of the ARAIM with SOP framework in an urban environment. The framework predicts conservative HPLs using ray-tracing simulations with 3D city models. The availability of high quality 3D models has enabled the performance evaluation of GNSS in urban canyons [24]. Ray-tracing has been utilized to predict signal propagation and visibility in mobile and wireless communication systems, and to estimate multipath and NLOS biases [25]. Conservative HPLs were also predicted for GPS only using ray-tracing simulations. Due to 3D map imperfections and other perturbations that arise in practice, e.g., signal blockage by foliage and surrounding vehicles, predicting the exact HPL of an AGV at a certain location and time is practically impossible. Therefore, this article predicts conservative HPLs by producing an upper bound for multipah and NLOS biases.

A flow chart for predicting the conservative HPLs is shown in Fig. 1. The proposed method first uses ray-tracing software, e.g., Wireless Insite, to simulate the channel impulse response (CIR) between each point on the map and the GNSS satellites or LTE base stations. The bias bounds are estimated from the CIRs using the methods described in the following subsections. Finally, FDE is conducted using the bias bounds and conservative HPLs are calculated accordingly.

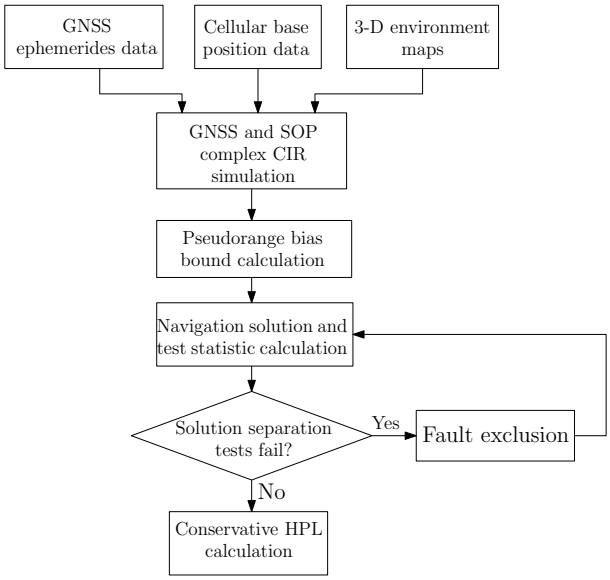

Fig. 1: Flowchart of proposed GNSS+SOP ARAIM.

A. GNSS Pseudorange Bias Prediction

Multipath/NLOS bias due to signal reflection and/or blockage by surrounding buildings is captured by $b_{\text{GNSS}_m}(k)$ in (1), which was predicted through ray-tracing simulations with a 3D building map. This term can be modeled as [26]

$$b_{\text{GNSS}_m}(k) = b_{\text{NLOS}_m}(k) + b_{\text{multipath}_m}(k), \tag{7}$$

where $b_{\text{NLOS}_m}(k)$ denotes the extra traveled distance between the reflected path and direct path when only NLOS signals are received and $b_{\text{multipath}_m}(k)$ denotes a bias caused by multipath. Note that in line-of-sight (LOS) conditions, $b_{\text{NLOS}_m}(k)$ becomes zero.

When the satellite positions, receiver position, and the 3D building map are given, the reflected paths can be simulated by finding the reflection point on the 3D building model using ray-tracing simulation. The position of the satellites at a specific time can be calculated from almanac data. The direct path can be determined by simply calculating the distance between satellites and the receiver. When there are multiple reflected paths, $b_{\text{NLOS}_m}(k)$ is calculated from the shortest reflected path.

If the ground vehicle receives multiple reflected signals, a multipath bias $b_{\text{multipath}_m}(k)$ can occur. The amount of multipath bias is determined by the correlator design of the code tracking loop in the receiver. In this paper, the *a posteriori* multipath estimation (APME) method [27] is assumed to be used for correlator design, and the multipath error is estimated using its noise envelope. The noise envelope is a function of the difference in traveled distance, received amplitude, and phase between the reflected and direct path. The multipath bias $b_{\text{NLOS}_m}(k)$ is modeled as

$$\begin{aligned} b_{\text{multipath}_m}(k) = \text{N}E(&R_{\text{reflected}_m}(k) - R_{\text{direct}_m}(k), \\ &A_{\text{reflected}_m}(k) - A_{direct_m}(k), \\ &\phi_{\text{reflected}_m}(k) - \phi_{\text{direct}_m}(k)), \end{aligned} \tag{8}$$

where $NE(\cdot)$ denotes the noise envelope function of the APME method (details are given on [27]); R denotes the simulated signal's traveled distance; A denotes the simulated received signal amplitude; ϕ denotes the simulated received signal phase; and subscript $_{\text{reflected}}$ and $_{\text{direct}}$ denote the reflected path and direct path, respectively. The time-of-arrival (TOA), received signal amplitude, and received signal phase were simulated by ray-tracing simulation and used to calculate the $b_{\text{multipath}_m}(k)$. Considering the possible blockage of GNSS signals by nearby vehicles, an elevation mask of 25° was conservatively set for the calculation.

B. SOP Pseudorange Bias Prediction

The bias term in (4) can be expressed as

$$b_{\text{SOP}_n}(k) = c \cdot \tau(k,0) - d_{\text{LOS}} + \chi_1(k) + \chi_2(k), \qquad (9)$$

where $c{\cdot}\tau(k,0)$ denotes the TOA of the first path; d_{LOS} is the LOS path length; and $\chi_1(k)$ and $\chi_2(k)$ are the biases due to multipath [28]. When the LOS signal is completely blocked or severely attenuated, the first path will be a reflected path. Therefore, $c \cdot \tau(k,0)$ will be larger than the true distance between the receiver and the LTE base station. As such, the pseudorange bias caused by NLOS effects becomes the difference between $c \cdot \tau(k,0)$ and d_{LOS}.

The complex CIR at the vehicle's position at time-step k can be modeled as [28]

$$r(k,\tau) = \sum_{l=0}^{L-1} \alpha(k,l)\delta(\tau - \tau(k,l)), \qquad (10)$$

where L is the number of multipath components; $\alpha(k,l)$ and $\tau(k,l)$ are the relative attenuation and delay components, respectively, of the l-th path with respect to the first path; and $\delta(\cdot)$ is the Dirac delta function. As Fig. 1 shows, the CIR can be simulated by ray-tracing with using a 3D building map, LTE base station locations and LTE signal properties.

The NLOS error and multipath interference can be predicted based on the simulated CIR. For the NLOS error, if the first simulated path is the LOS path, the NLOS error will be zero. Otherwise, the NLOS error is the difference between the delay for the first reflected path and LOS path.

Note that the effect of the delay of the reflected signal, $\tau(l)$, can be constructive or destructive. As the wavelength of LTE signals is only decimeters, small imperfections in the 3D models can induce large perturbations in the phase of $\alpha(l)$. Monte Carlo simulations are performed to calculate a pseudorange bias bound. For each Monte Carlo realization, the phase of $\alpha(l)$ is perturbed by $\Delta\phi \sim \mathcal{U}(-\pi,\pi)$. The relative amplitude $|\alpha(l)|$ is not varied in the Monte Carlo simulation, because it is assumed that the perturbation of amplitude due to map imperfections is relatively small. The bias bound is set to the maximum absolute bias out of all the Monte Carlo simulations.

IV. Simulation and Experimental Results

This section analyzes the performance of the proposed framework with SOP and multi-constellation GNSS signals.

A. Simulation Results

This subsection characterizes the integrity performance for the navigation system with GPS, GLONASS, and LTE pseudorange measurements. A simulation study was conducted on an area located in Riverside, CA, USA. The CIRs and conservative HPLs are simulated for a grid of locations with the resolution of 5 meters. The number of subcarrier symbols in the LTE pilot signal, was set to $B = 200$ with a bandwidth of 20 MHz and the time shift in the tracking loop was set to 0.5. The cell-specific reference signal (CRS) was used as the pilot signal [28]. The time epoch for the simulation is assumed to be 3:53 AM, on June 23rd 2018 UTC. As Fig. 2 (a) shows, there are 5 LTE base stations available in this area. Commercial 3D city maps (e.g., Fig. 2 (b)) from 3dbuildings [29] and ray-tracing software, Wireless Insite [30], are used to simulate the CIRs. Fig. 3 shows the CIR for the signal coming from transmitter 5 at the receiver position showing in Fig. 2. The upper bounds of the the pseudorange biases are further predicted using the method introduced in Section III. As an example, the pseudorange biases for transmitter 5 are plotted in Fig. 4. Finally, the conservative HPLs are further calculated by the ARAIM+SOP framework.

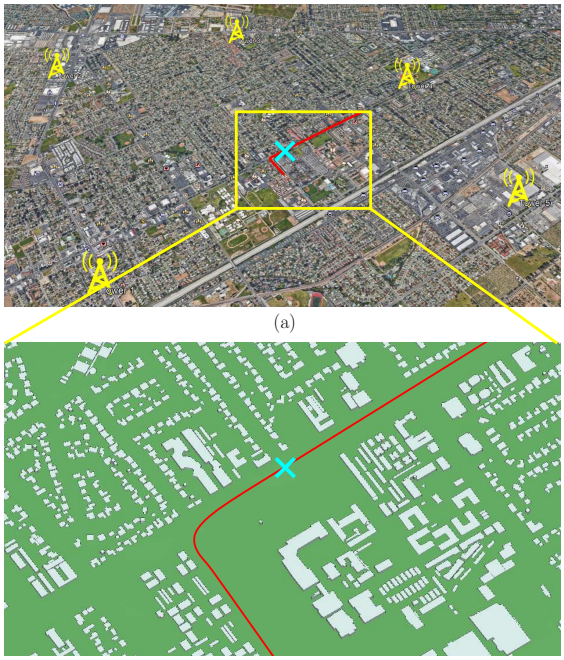

(a)

(b)

Fig. 2: (a) Simulation and experiment environment showing LTE tower locations and (b) 3D map of simulation environment. The receiver location is marked by an "X" for which the CIR is shown in Fig. 3. The vehicle trajectory is shown in red.

The parameters for the ARAIM+SOP framework are tabulated in Table I. Four scenarios of signal availability are considered in this paper: (i) GPS-only; (ii) GPS+GLONASS; (iii) GPS+SOP; and (iv) GPS+GLONASS+SOP. There are 11 GPS satellite and 7 GLONASS satellites available above the elevation mask during the simulation period. After FDE, the HPLs for the above four scenarios are plotted in Fig. 5.

Two conclusions can be drawn from Fig. 5. First, adding

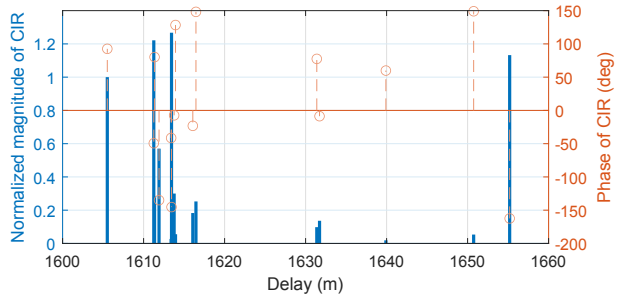

Fig. 3: CIR of the signal from transmitter 5 at the receiver position marked by an "X" in Fig. 2. The x-axis is the path delay expressed in meters.

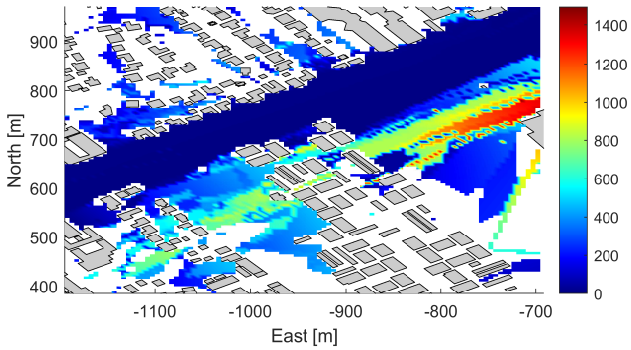

Fig. 4: Predicted range bias for transmitter 5.

the GLONASS and/or SOP will reduce the HPLs at some certain area. Second, adding GNSS or SOP constellations can reduce the availability. This is because that the ARAIM+SOP framework considers NLOS and large multipath biases as outliers to be detected. In urban environments, the NLOS and multipath errors could be common, which makes the probability of fault larger than the value used in the framework. As a result, there are scenarios where the number of simultaneous faults surpasses the maximum number of faults. For these scenarios, the measurement consistency will not satisfy the requirements after the FDE. The RAIM will consider the system as unavailable. There are two techniques to solve the problem of reduced availability. First, the integrity parameters can be characterized based on experiment campaigns in urban environments. Second, receivers can apply strategies to decide which constellation to use for navigation based on integrity maps.

B. Experimental Results

An experiment was conducted to demonstrate the proposed framework. In this experiment, a ground vehicle was equipped with two consumer-grade 800/1900 MHz cellular omnidirectional Laird antennas to receive the LTE signals. A National Instruments (NI) dual-channel universal software radio peripheral (USRP) 2954R, driven by a GPS disciplined oscillator (GPSDO) was used to down-mix and sample LTE signals. A Septentrio AsteRx-i V integrated GNSS-IMU sensor was used to provide the ground-truth trajectory. The ground vehicle traveled along a trajectory shown in Fig. 2.

TABLE I: RAIM Parameters

Parameter	Definition	Value
$\{\sigma_{URA,GNSS_m}\}_{m=1}^{M}$	User Range Error for GNSS	1 m
$\{\sigma_{URA,SOP_n}\}_{n=1}^{N}$	User Range Error for SOP	1 m
$PHMI_{HOR}$	Integrity budget for the horizontal component	10^{-7}
$PHMI_{VERT}$	Integrity budget for the vertical component	10^{-9}
PFA_{HOR}	Continuity budget allocated to the vertical component	10^{-7}
PFA_{VERT}	Continuity budget allocated to the vertical component	10^{-9}
$\{P_{GNSS_m}\}_{m=1}^{M}$	Probability of a single GNSS satellite fault	10^{-5}
$\{P_{SOP_n}\}_{n=1}^{N}$	Probability of a single SOP fault	10^{-4}

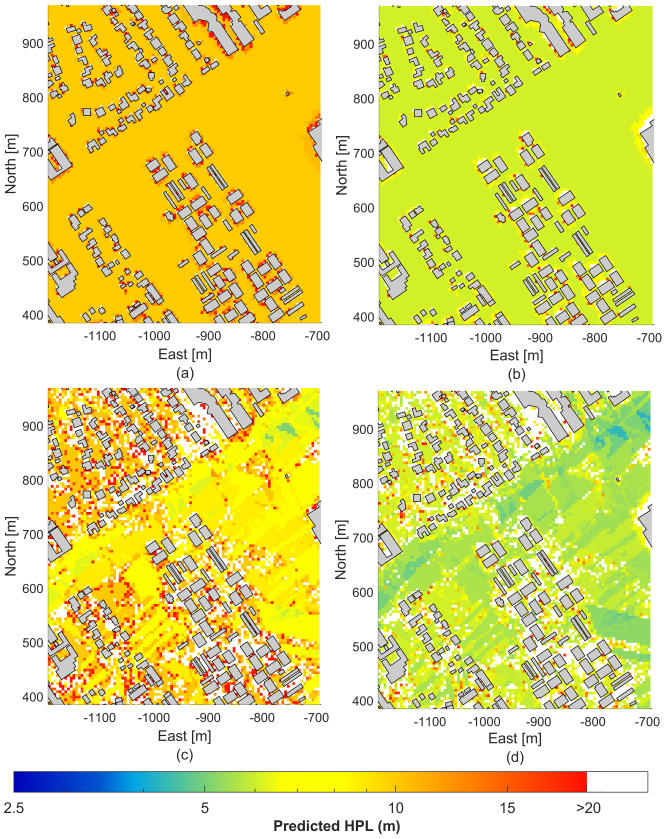

Fig. 5: Maps of conservatively predicted HPL for different navigation constellations: (a) GPS-only; (b) GPS+GLONASS; (c) GPS+SOP; (d) GPS+GLONASS+SOP.

The HPLs along the trajectory are plotted in Fig. 6. The horizontal alarm limit (HAL) is set to 20 m. It can be seen that (i) incorporating GLONASS and SOP pseudorange measurements reduces the HPLs and (ii) adding SOPs can be more effective than adding GLONASS in terms of reducing HPLs. For most of the trajectory, the HPL for GPS+SOP is smaller than GPS+GLONASS. It is worth highlighting that it is unfair to compare GLONASS with SOPs, as there were 7 GLONASS satellites available while only 5 SOPs were available during the experiment. Along the course of this experiment, the availability rates for GPS-only, GPS+GLONASS, GPS+SOP, and GPS+SOP+GLONASS were calculated to be 52.53%, 75.66%, 76.87%, and 80.72%, respectively.

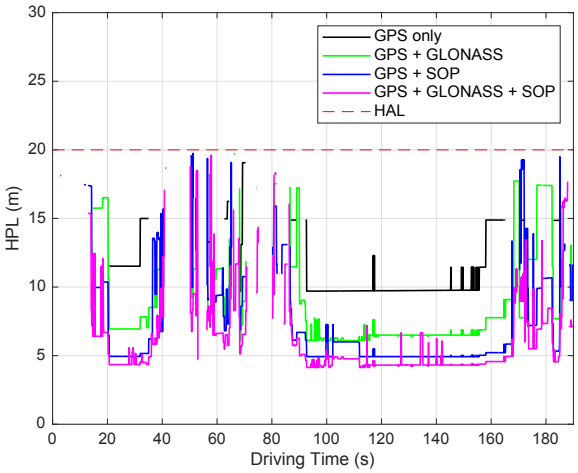

Fig. 6: HPLs over the course of the experiment trajectory. The HPL values above the HAL are truncated from the plot.

V. Conclusion

This paper proposed an ARAIM+SOP framework with multi-constellation GNSS and LTE pseudorange measurements for ground vehicle navigation. A method to predict conservative HPLs based on ray-tracing was introduced to produce the integrity map. Simulation and experiment results show that by incorporating multi-constellation GNSS and SOP pseudoranges, the HPLs are reduced. Experimental results for a ground vehicle navigating in an urban environment, showed the availability rates for GPS-only, GPS+GLONASS, GPS+SOP, and GPS+GLONASS+SOP to be 52.53%, 75.66%, 76.87%, and 80.72%, respectively.

References

[1] N. Zhu, D. Betaille, J. Marais, and M. Berbineau, "GNSS integrity monitoring schemes for terrestrial applications in harsh signal environments," *IEEE Intelligent Transportation Systems Magazine*, vol. 12, no. 3, pp. 81–91, 2020.

[2] T. Humphreys, M. Murrian, and L. Narula, "Deep-urban unaided precise global navigation satellite system vehicle positioning," *IEEE Intelligent Transportation Systems Magazine*, vol. 12, no. 3, pp. 109–122, 2020.

[3] D. Imparato, A. El-Mowafy, and C. Rizos, "Integrity monitoring: From airborne to land applications," in *Multifunctional Operation and Application of GPS*. IntechOpen, 2018, pp. 23–43.

[4] K. Nagai, T. Fasoro, M. Spenko, R. Henderson, and B. Pervan, "Evaluating GNSS navigation availability in 3-D mapped urban environments," in *Proceedings of IEEE/ION Position, Location and Navigation Symposium*, 2020, pp. 639–646.

[5] Z. Kassas, A. Abdallah, and M. Orabi, "Carpe signum: seize the signal – opportunistic navigation with 5G," *Inside GNSS Magazine*, vol. 16, no. 1, pp. 52–57, 2021.

[6] C. Yang, T. Nguyen, and E. Blasch, "Mobile positioning via fusion of mixed signals of opportunity," *IEEE Aerospace and Electronic Systems Magazine*, vol. 29, no. 4, pp. 34–46, April 2014.

[7] C. Yang and A. Soloviev, "Mobile positioning with signals of opportunity in urban and urban canyon environments," in *IEEE/ION Position, Location, and Navigation Symposium*, April 2020, pp. 1043–1059.

[8] Z. Kassas, J. Khalife, A. Abdallah, and C. Lee, "I am not afraid of the jammer: navigating with signals of opportunity in GPS-denied environments," in *Proceedings of ION GNSS Conference*, 2020, pp. 1566–1585.

[9] Z. Kassas, M. Maaref, J. Morales, J. Khalife, and K. Shamaei, "Robust vehicular localization and map matching in urban environments through IMU, GNSS, and cellular signals," *IEEE Intelligent Transportation Systems Magazine*, vol. 12, no. 3, pp. 36–52, June 2020.

[10] N. Zhu, J. Marais, D. Betaille, and M. Berbineau, "GNSS position integrity in urban environments: A review of literature," *IEEE Transactions on Intelligent Transportation Systems*, vol. 19, no. 9, pp. 2762–2778, September 2018.

[11] J. Blanch, T. Walter, P. Enge, Y. Lee, B. Pervan, M. Rippl, and A. Spletter, "Advanced RAIM user algorithm description: Integrity support message processing, fault detection, exclusion, and protection level calculation," in *Proceedings of ION GNSS Conference*, September 2012, pp. 2828–2849.

[12] J. Blanch, T. Walter, P. Enge, S. Wallner, F. Amarillo Fernandez, R. Dellago, R. Ioannides, I. F. Hernandez, B. Belabbas, A. Spletter *et al.*, "Critical elements for a multi-constellation advanced RAIM," *NAVIGATION, Journal of the Institute of Navigation*, vol. 60, no. 1, pp. 53–69, 2013.

[13] A. Ene, J. Blanch, and T. Walter, "Galileo-GPS RAIM for vertical guidance," in *Proceedings of National Technical Meeting of The Institute of Navigation*, January 2006, pp. 18–20.

[14] T. Walter, J. Blanch, M. J. Choi, T. Reid, and P. Enge, "Incorporating GLONASS into aviation RAIM receivers," in *Proceedings of International Technical Meeting of the Institute of Navigation*, January 2013, pp. 239–249.

[15] Y. Liu, J. Zhang, R. Xue, and Z. Wang, "Performance analysis of advanced RAIM with the inclusion of BeiDou," in *Proceedings of ION International Technical Meeting*, 2014, pp. 3629–3636.

[16] P. Roysdon and J. Farrell, "GPS-INS outlier detection and elimination using a sliding window filter," in *Proceedings of American Control Conference*, May 2017, pp. 1244–1249.

[17] T. Li, L. Pei, Y. Xiang, Q. Wu, S. Xia, L. Tao, X. Guan, and W. Yu, "P3-LOAM: PPP/LiDAR loosely coupled SLAM with accurate covariance estimation and robust RAIM in urban canyon environment," *IEEE Sensors Journal*, vol. 21, no. 5, pp. 6660–6671, 2021.

[18] L. Fu, J. Zhang, R. Li, X. Cao, and J. Wang, "Vision-aided RAIM: A new method for GPS integrity monitoring in approach and landing phase," *Sensors*, vol. 15, no. 9, pp. 22 854–22 873, 2015.

[19] M. Maaref and Z. Kassas, "Measurement characterization and autonomous outlier detection and exclusion for ground vehicle navigation with cellular signals," *IEEE Transactions on Intelligent Vehicles*, vol. 5, no. 4, pp. 670–683, December 2020.

[20] M. Maaref and Z. Kassas, "Autonomous integrity monitoring for vehicular navigation with cellular signals of opportunity and an IMU," *IEEE Transactions on Intelligent Transportation Systems*, 2021, accepted.

[21] M. Maaref, J. Khalife, and Z. Kassas, "Enhanced safety of autonomous driving by incorporating terrestrial signals of opportunity," in *Proceedings of IEEE International Conference on Acoustics, Speech and Signal Processing*, May 2020, pp. 9185–9189.

[22] M. Jia, J. Khalife, and Z. Kassas, "Evaluation of ground vehicle protection level reduction due to fusing GPS with faulty terrestrial signals of opportunity," in *Proceedings of ION International Technical Meeting*, January 2021, pp. 354–365.

[23] J. Khalife and Z. Kassas, "Precise UAV navigation with cellular carrier phase measurements," in *Proceedings of IEEE/ION Position, Location, and Navigation Symposium*, April 2018, pp. 978–989.

[24] L. Wang, P. Groves, and M. Ziebart, "Multi-constellation GNSS performance evaluation for urban canyons using large virtual reality city models," *Journal of Navigation*, vol. 65, pp. 459–476, 2012.

[25] N. Ziedan, "Urban positioning accuracy enhancement utilizing 3-D buildings model and accelerated ray tracing algorithm," in *Proceedings of ION GNSS Conference*, September 2017, pp. 3253–3268.

[26] G. Zhang and L. Hsu, "A new path planning algorithm using a GNSS localization error map for UAVs in an urban area," *Journal of Intelligent and Robotic Systems*, vol. 94, pp. 219–235, 2019.

[27] J. Sleewaegen and F. Boon, "Mitigating short delay multipath: a promising new technique," in *Proceedings of ION International Technical Meeting Conference*, September 2010, pp. 204–213.

[28] K. Shamaei and Z. Kassas, "LTE receiver design and multipath analysis for navigation in urban environments," *NAVIGATION, Journal of the Institute of Navigation*, vol. 65, no. 4, pp. 655–675, December 2018.

[29] "3dbuildings," https://3dbuildings.com.

[30] Remcom Inc., "Wireless insite," https://www.remcom.com/.